



Spatiotemporal Propagation of the Cortical Atrophy: Population and Individual Patterns

OPEN ACCESS

Edited by:

Yasser Iturria Medina,
McGill University, Canada

Reviewed by:

Alexandra Young,
University College London,
United Kingdom
Bruno Michel Jedynak,
Portland State University,
United States

*Correspondence:

Igor Koval
igor.koval@icm-institute.org

[†]Data used in preparation of this article were obtained from the Alzheimer's Disease Neuroimaging Initiative (ADNI) database (adni.loni.usc.edu). As such, the investigators within the ADNI contributed to the design and implementation of ADNI and/or provided data but did not participate in analysis or writing of this report. A complete listing of ADNI investigators can be found at: http://adni.loni.usc.edu/wp-content/uploads/how_to_apply/ADNI_Acknowledgement_List.pdf

Specialty section:

This article was submitted to Neurodegeneration, a section of the journal *Frontiers in Neurology*

Received: 28 July 2017

Accepted: 26 March 2018

Published: 04 May 2018

Citation:

Koval I, Schiratti J-B, Routier A, Bacci M, Colliot O, Allassonnière S and Durrleman S (2018) Spatiotemporal Propagation of the Cortical Atrophy: Population and Individual Patterns. *Front. Neurol.* 9:235. doi: 10.3389/fneur.2018.00235

Igor Koval^{1,2*}, Jean-Baptiste Schiratti^{1,2}, Alexandre Routier¹, Michael Bacci¹, Olivier Colliot^{1,3,4}, Stéphanie Allassonnière² and Stanley Durrleman¹ for the Alzheimer's Disease Neuroimaging Initiative[†]

¹Inria Paris-Rocquencourt, INSERM U1127, CNRS UMR 7225, Sorbonne Universités, UPMC Univ Paris 06 UMRS 1127, Institut du Cerveau et de la Moelle épinière, ICM, Paris, France, ²INSERM UMRS 1138, Centre de Recherche des Cordeliers, Université Paris Descartes, Paris, France, ³AP-HP, Pitié-Salpêtrière Hospital, Department of Neurology, Paris, France, ⁴AP-HP, Pitié-Salpêtrière Hospital, Department of Neuroradiology, Paris, France

Repeated failures in clinical trials for Alzheimer's disease (AD) have raised a strong interest for the prodromal phase of the disease. A better understanding of the brain alterations during this early phase is crucial to diagnose patients sooner, to estimate an accurate disease stage, and to give a reliable prognosis. According to recent evidence, structural alterations in the brain are likely to be sensitive markers of the disease progression. Neuronal loss translates in specific spatiotemporal patterns of cortical atrophy, starting in the entorhinal cortex and spreading over other cortical regions according to specific propagation pathways. We developed a digital model of the cortical atrophy in the left hemisphere from prodromal to diseased phases, which is built on the temporal alignment and combination of several short-term observation data to reconstruct the long-term history of the disease. The model not only provides a description of the spatiotemporal patterns of cortical atrophy at the group level but also shows the variability of these patterns at the individual level in terms of difference in propagation pathways, speed of propagation, and age at propagation onset. Longitudinal MRI datasets of patients with mild cognitive impairments who converted to AD are used to reconstruct the cortical atrophy propagation across all disease stages. Each observation is considered as a signal spatially distributed on a network, such as the cortical mesh, each cortex location being associated to a node. We consider how the temporal profile of the signal varies across the network nodes. We introduce a statistical mixed-effect model to describe the evolution of the cortex alterations. To ensure a spatiotemporal smooth propagation of the alterations, we introduce a constrain on the propagation signal in the model such that neighboring nodes have similar profiles of the signal changes. Our generative model enables the reconstruction of personalized patterns of the neurodegenerative spread, providing a way to estimate disease progression stages and predict the age at which the disease will be diagnosed. The model shows that, for instance, APOE carriers have a significantly higher pace of cortical atrophy but not earlier atrophy onset.

Keywords: Alzheimer's disease, cortical atrophy, brain networks, spatiotemporal propagation patterns, individual variability

1. INTRODUCTION

Neuroimaging studies have shown an alteration of the brain structure during the course of Alzheimer's disease (AD) (1, 2). These lesions appear during the prodromal phase of the disease (3–5) whose observation have been limited due to the absence of clinical symptoms and diagnosis. The importance of the structural changes before the clinical symptoms led to hypothetical models (6), which have been later refined thanks to the gathering of multiple scientific evidences. These modifications took the form of a structural change of the brain in particular an important neuronal loss and an atrophy of the brain cortex (7, 8). The study of the temporal evolution of the cerebral cortex reveals an atrophy of the gray matter (9). This cortical atrophy presumably relates the traces of the progression of the lesions over the brain surface. A fine-scale modeling of the atrophy propagation is likely to give a wider understanding of the disease evolution, as the structural markers seems reliable to assess the conversion to the AD stage, potentially carrying subtle indicators of the disease progression in early phases.

The spatiotemporal propagation of these alterations encloses two entangled components. On the one hand, the spatial characterization of the lesions over the brain surface at each time, and, on the other hand, a temporal dynamic of these alterations that may differ from one region to another. Characterizing the proper dynamics of these lesions relies on the possibility to reconstruct the whole time-line of AD, at both a spatial and temporal level, out of short-term observations that are not temporally aligned. Another challenging aspect consists in the variability inherent to the individual patterns of atrophy that requires to consistently compare the subject-specific spreads of alterations. Accounting for the interindividual variability in term of lesion propagation should allow to reconstruct individual patterns of propagation, paving the way to possible personalized model of atrophy, that potentially informs on subject-specific age of conversion or disease stage.

Recently, large datasets have opened the opportunity to investigate data-driven models that have refined and validated these hypotheses to some extent, in particular event-based models (10–12) that considers the propagation as a series of events, allowing to define a sequence of disease stages. They characterize the overall variability of the events ordering at a population level. However, these models are not well suited to relate for the temporal delays of the alterations at a population level, neither to determine individual cortical atrophy. Multimodal observations, including positron emission tomography (PET) scans, magnetic resonance imaging (MRI) and biomarkers, have been gathered within longitudinal databases, i.e., repeated observations of patients during significant periods of time. The underlying intention is to provide multiple individual snapshots of the disease—patients examined during short-term periods—in order to reconstruct the long-term history of the pathology (13, 14) at a group and individual level. Moreover, it offers the possibility to describe and interpret the observed data contrary to quantiles or percentiles that require arbitrary reference distributions. A challenging aspect of AD patient comparison is the fact that, even though AD is related to age, the latter is not a good proxy of the disease stage (15–17) leaving us without any

easy way to align all the individual on the same time-line. In Ref. (18), the authors introduced mixed-effect model that consider each individual trajectory as a variation of a mean scenario of evolution, with a time-warp function that is able to realign the subjects on the same time-line (19). It allows to characterize a spatial and temporal variability of propagation in the sense that it defines a group-average trajectory of propagation with the possibility to reconstruct individual observations thanks to personalized parameters. Nevertheless (18), constrain the model to parallel profiles of progression which does not hold when looking at signals that have various dynamics. Moreover, the model does not take into account the spatial correlations between the data whereas (17), which focus on spatiotemporal patterns of progression for images, exhibited that this led, in the case of a non-linear mixed-effects model, to poor estimations of the subject-specific parameters and individual trajectories.

To account for the spatial structure of the signal, networks have been introduced (20, 21), representing the brain areas as the graph nodes. In this paper, the networks correspond to a graph representation of a signal spatially distributed, namely, the cortical thickness mapped on a mesh representation of the cortex. The node values are the cortical thickness values over time on the related brain area. Extracting and projecting patients cortical thickness on the common mesh allows to compare their atrophy on the same atlas to exhibit similar patterns. As we expect the signal propagation to be spatially smooth with a similar temporal profile of change for neighbor nodes, we consider that a subset of the graph nodes act as control nodes. They define an evaluation function such that the signal at each node is an interpolation of the signal at the control nodes, enabling to smooth the high frequencies (22). The proximity between nodes is defined by the distance matrix which informs on the distance between any pair. Moreover, the number of nodes of this vertex-based graph can be tuned based on the desired application, potentially the same as the resolution of the input data, e.g., a voxel for MRI or PET data.

The aim of this paper is to introduce a model of the cortical atrophy propagation during the long-term course of AD thanks to a graph representation of the neuroimaging data. This model is able to personalize the reconstruction of the propagation to individual longitudinal measurements, allowing to describe the stages of the disease, potentially in the future. The model is described as a general framework for any longitudinal data spatially distributed on a common graph and it is instantiated to exhibit the propagation of the cortical atrophy on the left hemisphere of the brain, across nearly 2000 regions, thanks to longitudinal observations of 154 mild cognitive impaired (MCI) patients that were later diagnosed with AD. While exhibiting an average pattern of propagation, this mixed-effects model allows to reconstruct individual observations through time.

2. MATERIALS AND METHODS

2.1. Sketch of the Method

Prior to detail our method, we would like to sketch the key ideas and notations of our work to ease and guide the reading. First, we consider I patients; each patient i is observed J_i times, his j th visit

being at age t_{ij} , and each observation led to an MRI scan as shown on the left hand side of **Figure 1**. Segmentation of the cortical thickness, out of the neuroimaging observations, are mapped onto a mesh, as presented on the middle part of **Figure 1**. The last step corresponds to a subsampling process that led to a graph G of K nodes, characterized by a distance matrix D . At each node, the individual observations define a time-series describing the evolution of the signal through time.

In a second time, we assume that, at each node k of the graph G , there exists a function $t \mapsto \gamma_k(t)$ that describes a characteristic evolution of the signal at this node, as shown on **Figure 2**. The time-series of individual i at node k derives from a continuous function $\eta_{ik}(t)$, which is assumed to be a spatial and temporal variations of the representative trajectory $\gamma_k(t)$, illustrated on **Figure 3**. The temporal variation corresponds to the time realignment of individual i on the common time-line. It adjusts the individual dynamics to a mean pace of evolution, thanks to personalized parameters τ_i and α_i . τ_i stands for the individual time-shift to the mean disease onset, allowing an early ($\tau_i < 0$) or delayed ($\tau_i > 0$) age at diagnosis. The parameter α_i integrates the patient-specific possibility to have a faster ($\alpha_i > 1$) or slower ($\alpha_i < 1$) pace of atrophy compared to the mean scenario of changes. On the other side, the spatial variation corresponds to the adjustment from the mean cortical thickness to individual data. It accounts, for instance, for the difference in size or in spatial thickness distribution at the same disease stage.

We consider that the characteristic signal $\gamma_k(t)$ at node k belongs to a family of curve, here the straight line curves, parametrized by the cortical thickness p_k and the rate of atrophy v_k . To account for the spatial structure of the signal and the large number of nodes, a subset of nodes, referred to as control nodes, is selected to control the interpolation of the cortical and atrophy values over all the nodes. The distribution of the control nodes depends on the size of the kernel bandwidth such that the kernels densities map almost uniformly the feature space.

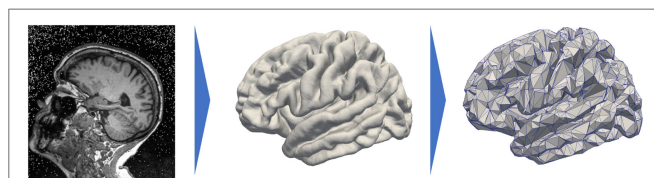


FIGURE 1 | Data preprocessing that projects the cortical thickness of the raw MRI observation (left) on a mesh, namely, the FSAverage atlas constituted of 163,842 nodes per hemisphere (middle) before subsampling it and averaging the signal onto a 1,827-node graph (right).

The model introduces population parameters, that allow to define a characteristic spatiotemporal trajectory of the atrophy, and individual parameters, that not only enable to reconstruct individual trajectories but also permit the statistical study of the distribution of spatiotemporal atrophy patterns. These parameters are estimated thanks to the Monte-Carlo Markov-Chain Stochastic Approximation Expectation-Maximization (MCMC-SAEM) algorithm, which handles non-linear mixed-effects models, with theoretical guarantees and consistent results in practice.

2.2. Subjects and Data Preprocessing

Data used in the preparation of this article were obtained from the Alzheimer's Disease Neuroimaging Initiative (ADNI) database (adni.loni.usc.edu). The ADNI was launched in 2003 as a public-private partnership, led by Principal Investigator Michael W. Weiner, MD. The primary goal of ADNI has been to test whether serial magnetic resonance imaging (MRI), positron emission tomography (PET), other biological markers, and clinical and neuropsychological assessment can be combined to measure the progression of mild cognitive impairment (MCI) and early Alzheimer's disease (AD). For up-to-date information, see www.adni-info.org.

The Alzheimer's Disease Neuroimaging Initiative (ADNI) dataset contains longitudinal MRI data for patients that are, at each visit, either cognitively normal (CN), mild cognitive impaired (MCI) patients, or, AD subjects. We selected all the subjects that presented a monotonous decline from MCI to AD, called the MCI converters, removing those that may convert from AD back to MCI or CN. Although AD patients get through an MCI phase, we could not keep CN to MCI patients as they might just as well convert to another dementia. Also, the patients that underwent from CN to MCI and then to AD are not numerous enough to give robust estimation of early stages (CN to MCI). Thus, we kept only the MCI to AD visits of such patients. Altogether, the paper focuses on 154 MCI patients that represents 787 visits, each individual being examined 5 times on average, from 2 to 7 times.

Each visit led to a T1-weighted MRI acquisition, as shown on the left side of **Figure 1**. The longitudinal pipeline of FreeSurfer (23) was used to extract the cortical thickness of the left hemisphere of the brain which was then projected on a common atlas, namely, FSAverage (24), which is a three-dimensional mesh composed of 163,842 nodes for each hemisphere represented on the central part of **Figure 1**. This common fixed-graph allows to compare the cortical thickness between visits or patients, node to node.

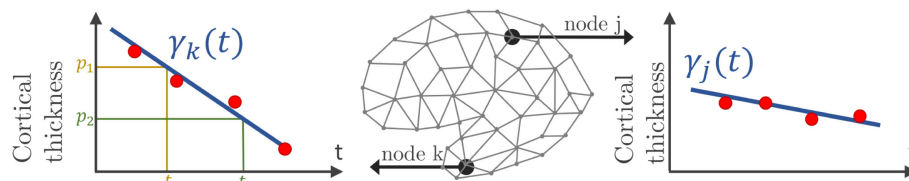


FIGURE 2 | Mesh of the cortical surface where each node embeds a time-series of observations (red points). At node k , the function $\gamma_k(t)$, which can be parametrized by a velocity and two different sets (ρ_1, t_1) or (ρ_2, t_2) , estimates the cortical thickness over time.

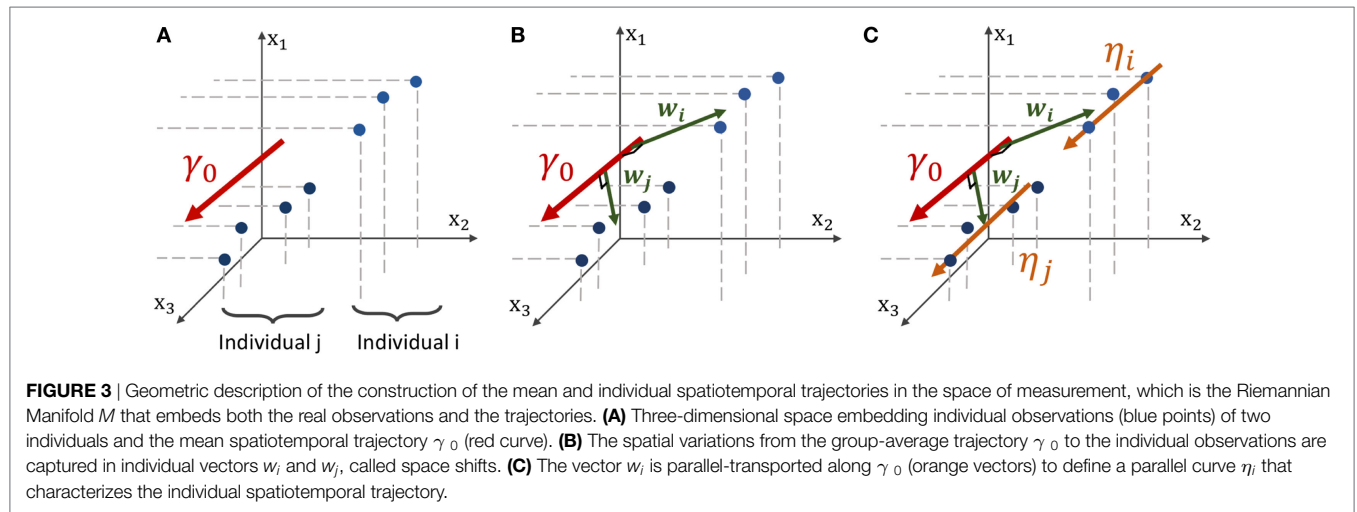


FIGURE 3 | Geometric description of the construction of the mean and individual spatiotemporal trajectories in the space of measurement, which is the Riemannian Manifold M that embeds both the real observations and the trajectories. **(A)** Three-dimensional space embedding individual observations (blue points) of two individuals and the mean spatiotemporal trajectory γ_0 (red curve). **(B)** The spatial variations from the group-average trajectory γ_0 to the individual observations are captured in individual vectors w_i and w_j , called space shifts. **(C)** The vector w_i is parallel-transported along γ_0 (orange vectors) to define a parallel curve η_i that characterizes the individual spatiotemporal trajectory.

The data acquisition and interindividual alignment led to a considerable noise, especially in terms of variability in the measures for close nodes. To smooth this noise and to reduce the computational time, we subsampled the initial graph into a new graph of 1,827 nodes. To do so, we selected 1,827 nodes uniformly distributed over the whole FSAverage graph; the other nodes were then associated to one of the 1,827 nodes thanks to a geodesic distance d on the graph (i.e., the length of the shortest path on the surface mesh between the nodes) using the Fast Marching Algorithm on the mesh (25). Therefore, it constitutes collection of nodes referred to as patches. The value of each node of the subsampled graph is the average value over the corresponding patch, each being constituted of approximately 89 initial nodes of the FSAverage graph. The resolution of this vertex-based approach is lower than the initial one, shown on the right hand side of **Figure 1**, but still holds the brain topology while smoothing part of the acquisition noise. In our case, each observation can be considered as a vector of size 1,827 where the k th coordinate is related to the k th node of the common fixed-graph G . The latter is also described by the distance matrix D between the 1,827 nodes. It was obtained using the geodesic distance d between the 1,827 nodes on the initial graph FSAverage, whose edges are weighted by a physical length. Finally, for all $i, j \in \{1, \dots, 1,827\}$, we set $D_{ij} = d(\mathbf{x}_i, \mathbf{x}_j)$ where \mathbf{x}_i and \mathbf{x}_j are two nodes of the graph.

In the following, we will present a data-driven model which allow to track the propagation of any signal spatially distributed, supposedly the cortical thickness. We consider a longitudinal dataset $\mathbf{y} = (\mathbf{y}_{ij})_{1 \leq i \leq I, 1 \leq j \leq J_i}$ of I individuals, each patient i being observed J_i times during the study at ages $(t_{ij})_{1 \leq j \leq J_i}$. We suppose that there exist a common fixed-graph G defined by a set $\mathcal{V} = (\mathbf{x}_1, \dots, \mathbf{x}_K)$ of K nodes and a distance matrix D which accounts for the distance between the nodes. Any node $\mathbf{x}_k \in \mathbb{R}^3$ corresponds to a coordinate of a point in space. Each observation $\mathbf{y}_{ij} = (\mathbf{y}_{ij1}, \dots, \mathbf{y}_{ijK}) \in \mathbb{R}^k$ corresponds to the measured signal spatially distributed over the N nodes of G , represented by a point in the multivariate space \mathbb{R}^k , schematically represented on **Figure 3A** for $K = 3$, as if there were only 3 vertices in the mesh. Therefore, it defines a network whose nodes are valued with the signal of interest. It follows that the collection $(\mathbf{y}_{ij})_{1 \leq j \leq J_i}$ of the

observations of a particular subject defines a network that embeds a time-series on each node of G , indexed by the patient age at each observation $(t_{ij})_{1 \leq j \leq J_i}$.

2.3. Model

2.3.1. From Short-Term Data to Long-Term History

We assume there that the repeated observations of a subject are sampled from a continuous function $t \mapsto \eta_i(t) = (\eta_{i1}(t), \dots, \eta_{iN}(t))$, where $\eta_{ik}(t)$ describes the decrease of cortical thickness of this i th individual at vertex k , such that

$$\forall i \in \{1, \dots, I\} \quad \forall j \in \{1, \dots, J_i\} \quad \forall k \in \{1, \dots, K\}$$

$$y_{ijk} = \eta_{ik}(t_{ij}) + \epsilon_{ijk}, \tag{1}$$

where $\epsilon_{ijk} \sim N(0, \sigma^2)$ corresponds to the model noise, whose variance is σ^2 .

The function $t \mapsto \eta_{ik}(t)$ describes the evolution of the time-series at node k for the individual i . Thus, the vector function $t \mapsto \eta_i(t) = (\eta_{i1}(t), \dots, \eta_{iN}(t))$ describes the continuous evolution on the graph for a particular individual, i.e., the spatiotemporal propagation of the signal over the whole brain. It corresponds to a spatiotemporal trajectory in the space of measurements. The trajectory $t \mapsto \eta_i(t)$ is therefore able to reconstruct the existing observations $(\mathbf{y}_{ij})_{1 \leq j \leq J_i}$, defined at the related time-points $(t_{ij})_{1 \leq j \leq J_i}$, as shown on **Figure 3B**, but also generate an observation at any time t , potentially in the future.

The repeated data of each individual is a particular window in the long-term course of the disease that potentially overlaps with other patients. We aim to realign along a common time-line these short-term sequences by carefully analyzing the spatiotemporal patterns within each short-term snapshot. Nevertheless, to do so, we also need to account for the interindividual variability in cortical thickness measurements and trajectories of propagation across the network. The interindividual variability prevents us from considering any individual propagation as a good representation of the disease evolution.

Consequently, we assume that there exists a mean scenario of propagation, defined by a group-average spatiotemporal trajectory $t \mapsto \gamma_0(t)$, represented on **Figure 3C**, such that each individual trajectory $t \mapsto \eta_i(t)$ is a temporal and spatial variation of this

mean scenario of changes, detailed in section 2.3.2. This typical scenario of change describes the mean pattern of spatiotemporal propagation of the signal and writes $\gamma_0(t) = (\gamma_1(t), \dots, \gamma_K(t))$ where for all $k \in \{1, \dots, K\}$, $t \mapsto \gamma_k(t)$ characterize the typical temporal evolution of the cortical thickness on the brain region related to the node k . As represented in **Figure 2**, each node has a different temporal profile of atrophy, accounting for the variation of the cortical thickness over time.

2.3.2. Individual Estimation

Translating the generic framework introduced by Schiratti et al. (18) into this case requires to exhibit individual parameters that characterize the individual spatial and temporal variations to the mean, namely the *space shifting* and the *time reparametrization*.

2.3.2.1. Time Reparametrization

We introduce a time-warp function $\psi_i(t)$ that corresponds to a time reparametrization that adjust the individual dynamics on a common time-line, which here is the average spatiotemporal trajectory γ_0 . For any patient i with observations $(y_{ij})_{1 \leq j \leq n_i}$ at time-points $(t_{ij})_{1 \leq j \leq n_i}$, $\psi_i(t_{ij}) = \alpha_i(t_{ij} - t_0 - \tau_i) + t_0$ where t_0 is a common reference time of the reparametrization, α_i encodes for the individual pace of propagation and $t_0 + \tau_i$ describes subject-specific time-shift to the mean disease onset. As such, if the acceleration factor α_i is greater than 1, it corresponds to a faster pace of cortical atrophy whereas $\alpha_i < 1$ indicates a slower pace of atrophy. In the same way, the larger the value of the time-shift τ_i is, the later the disease occurs. Therefore, it leads to write $\eta_i(t) = \gamma_0(\psi_i(t)) + \epsilon_{ij}$. It adjusts the pace at which the trajectory is followed for the i th individual.

2.3.2.2. Space Shifting

In the space of measurements \mathbb{R}^K , we consider individual observations and the mean trajectory $\gamma_0(t)$ as shown in **Figure 3A**. In order to account for the spatial variability of the individual trajectories, we assume that there exists, for any individual i , a vector $w_i \in \mathbb{R}^K$ called the space shift, that characterizes the spatial variations from $\gamma_0(t)$ to the observations as shown in **Figure 3B**. For any point on $\gamma_0(t)$, $\gamma_0(t) + w_i$ is assumed to be on the individual trajectory. Therefore, it is possible to translate all the points $(\gamma_0(t))_{t \in \mathbb{R}}$ to $(\gamma_0 + w_i)_{t \in \mathbb{R}}$ as shown in **Figure 3C**. This collection defines the individual trajectory $\eta_i(t)$. This space shift must be orthogonal to the trajectory as it ensures the identifiability of the model. In fact, if the direction w_i was not orthogonal to the trajectory, then the projection of w_i on the geodesic γ_0 would interfere with the individual time realignment induced by the dynamic parameters (α_i, τ_i) .

Using mathematical tools from the Riemannian geometry beyond the scope of this study (26) shows that the k th coordinate of the individual spatiotemporal trajectory writes $\eta_{ik}(t) = \gamma_k(\frac{w_{ik}}{\dot{\gamma}_k(t_0)} + \psi_i(t))$. As the space shift must be estimated in \mathbb{R}^K , w_i is supposed to be a linear combination of few independent components, in the spirit of independent component analysis (ICA) (27). It leads to consider A a $K \times N_s$ matrix of N_s independent directions, and $(s_{ij})_{1 \leq i \leq K, 1 \leq j \leq N_s}$ parameters to estimate. $s_i = (s_{i1}, \dots, s_{iN_s}) \in \mathbb{R}^{N_s}$ correspond to parameters of individual i that characterize his spatial variations from the mean spatiotemporal

trajectory. The orthogonality condition, mentioned in the previous paragraph, leads to consider a basis $(B_1, \dots, B_{(K-1)N_s})$ of matrices, whose columns are orthogonal to the direction of $\gamma_0(t)$, and parameters $(\beta_l)_{1 \leq l \leq (K-1)N_s}$ such that $A = \sum_{j=1}^{(K-1)N_s} \beta_j B_j$. This procedure allows to reduce the dimension of the parameters to estimate for each w_i , from K to the chosen number of sources.

It leads to write:

$$y_{ijk} = \gamma_k \left(\frac{w_{ik}}{\dot{\gamma}_k(t_0)} + \alpha_i(t_{ij} - \tau_i - t_0) + t_0 \right) + \epsilon_{ijk}. \quad (2)$$

2.3.3. Curve Parametrization

In this paper, we consider a *straight line model* such that $\gamma_k(t) = v_k(t - t_k) + p_k$, v_k accounting for the ratio of atrophy and p_k for the thickness value at time t_k . A linear decay in cortical atrophy is then represented by a straight line trajectory, parametrized by time, in the K -dimensional space as shown on **Figure 3**. Note that as shown on **Figure 2**, it is possible to parametrize the same curve with two distinct sets (p_1, t_1) and (p_2, t_2) preventing from having an identifiable model. We decided to fix the parameter t_k among all the nodes such that for all $k \in \{1, \dots, K\}$ $t_k = t_0$, the time reference used in section 2.3.2.1, without any loss of generality as $t \mapsto \gamma_k(t)$ is defined on \mathbb{R} . Despite the linear form of each coordinate $t \mapsto \gamma_k(t)$, the resulting model is non-linear as it includes among others, multiplication of individual and population parameters.

Finally, equation (2) becomes

$$y_{ijk} = p_k + w_{ik} + v_k \alpha_i(t_{ij} - \tau_i - t_0) + \epsilon_{ijk}. \quad (3)$$

This model therefore defines a distribution of multivariate straight line trajectories that accounts for the distribution of the individual trajectories.

2.3.4. Spatial Smoothness

The model proposed in this paper deals with data that are spatially distributed on a graph G defined by a set of nodes $\mathcal{V} = (\mathbf{x}_1, \dots, \mathbf{x}_K)$, where each node embeds a spatial coordinate in \mathbb{R}^3 . We expect a smoothly varying profile of atrophy across nodes. The proximity between edges is given by the distance matrix D .

In order to ensure small variations of the signal, we introduce a subset $\mathcal{V}_c = (\mathbf{x}_{d_1}, \dots, \mathbf{x}_{d_{N_c}}) \subset \mathcal{V}$ whose vertices are called control nodes. Instead of estimating $(p_k)_{1 \leq k \leq K}$ (resp. $(v_k)_{1 \leq k \leq K}$) at all the nodes, we consider only the parameters at the control nodes $(p_{d_k})_{1 \leq k \leq N_c}$ (resp. $(v_{d_k})_{1 \leq k \leq N_c}$). We introduce an estimation function $\mathbf{x} \mapsto p(\mathbf{x})$ (resp. $\mathbf{x} \mapsto v(\mathbf{x})$) for all $\mathbf{x} \in \mathcal{V}$ such that, at the control nodes, the function is equal to the parameters: $\forall k \in \{1, \dots, N_c\}$, $p(\mathbf{x}_{d_k}) = p_{d_k}$ (resp. $v(\mathbf{x}_{d_k}) = v_{d_k}$). At the other nodes, the function is an interpolation of the parameter value at the control nodes weighted by the distance to each of them. Therefore, the control vertices control the evaluation of the parameters among all the nodes.

We choose a Gaussian kernel K_b as interpolation splines: $\forall x, y \in \mathcal{V}$, $K_b(x, y) = \exp(-\frac{d(x, y)^2}{b^2})$ where d is the geodesic distance on the mesh and b is the kernel bandwidth. This interpolation allows to remove the possible high frequencies, smoothing

the signal spatially. Therefore, it leads to write:

$$\forall \mathbf{x} \in \mathcal{V}, p(\mathbf{x}) = \sum_{i=1}^{N_c} \beta_p^i K_b(\mathbf{x}, \mathbf{x}_{d_i}) \quad \text{and}$$

$$\forall \mathbf{x} \in \mathcal{V}, v(\mathbf{x}) = \sum_{i=1}^{N_c} \beta_v^i K_b(\mathbf{x}, \mathbf{x}_{d_i}). \quad (4)$$

The parameters $(\beta_p^i)_{1 \leq i \leq N_c}$ (resp. $(\beta_v^i)_{1 \leq i \leq N_c}$) are the solution of the linear system $p^{d_k} = \sum_{i=1}^{N_c} \beta_p^i K_b(\mathbf{x}_{d_k}, \mathbf{x}_{d_i})$ (resp. $v^{d_k} = \sum_{i=1}^{N_c} \beta_v^i K_b(\mathbf{x}_{d_k}, \mathbf{x}_{d_i})$).

Given these interpolations, equation (3) writes

$$y_{ijk} = p(\mathbf{x}_k) + (As_i)_k + v(\mathbf{x}_k)\alpha_i(t_{ij} - \tau_i - t_0) + \epsilon_{ijk}. \quad (5)$$

Even though the distance computed for the cortical thickness corresponds to a distance on the brain cortex, it is possible to compute a connectivity distance based on the connectome, or even an appropriate combination of some of these distances. The challenging part is to put into correspondence areas defined by the connectivity matrices and other networks such as the FSAverage Atlas.

The choice of the set \mathcal{V}_c of control nodes among the whole set of nodes \mathcal{V} is mostly determined by the choice of the bandwidth b : their uniform distribution is such that there is an approximate distance b between them. In the case of the cortical thickness, we have chosen a bandwidth equal to 16 mm which is representative of the spatial variability of the signal.

2.4. Algorithm

Equation (5) describes a mixed-effects model, introducing population and individual parameter in this high-dimensional non-linear model. We consider that $((\alpha_i)_{1 \leq i \leq I}, (\tau)_{1 \leq i \leq I}, (s_{ij})_{1 \leq i \leq p, 1 \leq j \leq N_s})$ are random-effects of the model, leading to write $\forall i \in \{1, \dots, I\} \forall j \in \{1, \dots, N_s\}$:

$$\alpha_i = \exp(\xi_i), \xi_i \sim \mathcal{N}(0, \sigma_\xi^2), \tau_i \sim \mathcal{N}(0, \sigma_\tau^2), \text{ and,}$$

$$s_{ij} \sim \text{Laplace}\left(0, \frac{1}{2}\right). \quad (6)$$

α_i corresponds to the realization of a log-normal distribution so that it is always positive, preventing the individuals to present an increasing cortical thickness over time. Moreover, the Laplacian distribution of s_{ij} arises from theoretical considerations as we need the model to be identifiable, i.e., the solution of the problem to be unique. Finally, these random-effects account for the statistical distribution of the individual trajectories. In the following, we consider $\mathbf{z} = ((\alpha_i)_{1 \leq i \leq I}, (\tau)_{1 \leq i \leq I}, (s_{ij})_{1 \leq i \leq I, 1 \leq j \leq N_s})$ as hidden variables.

Given equation (5) and the observations \mathbf{y} , we would like to estimate the parameters $\theta = (t_0, (p^{d_k})_{1 \leq k \leq N_c}, (v^{d_k})_{1 \leq k \leq N_c}, (\beta_k)_{1 \leq k \leq N_c(K-1)}, \sigma_\tau, \sigma_\xi, \sigma)$ as a maximum likelihood estimate (MLE) $\theta^* = \text{argmax}_\theta p(\mathbf{y}|\theta)$. The natural way to perform such estimation in mixed-effects models is the Expectation-Maximization algorithm (28). Unfortunately, the E-step is intractable and it is not possible to sample according to the conditional distribution

ALGORITHM 1 | Estimation of the general and individual cortical thickness decrease with the MCMC-SAEM algorithm.

Input: Longitudinal dataset $y = (y_{ij})_{i,j}$ of measurement maps, with the corresponding ages $(t_{ij})_{i,j}$.
Initial parameters θ^0 and latent variables z^0 .
Geometrically decreasing sequence of step-sizes ρ^k .
Sufficient statistics S^k .

Initialization: set $k = 0$ and $S^0 = S(z^0)$.

repeat

Simulation: **foreach** block of latent variables z_b **do**
 Draw a candidate $z_b^c \sim p_b(\cdot | z_b^k)$.
 Set $z^c = (z_1^{k+1}, \dots, z_{b-1}^{k+1}, z_b^c, z_{b+1}^k, \dots, z_{n_b}^k)$.
 Compute the acceptance ratio $\omega = \min\left[1, \frac{q(z^c | y, \theta^k)}{q(z^k | y, \theta^k)}\right]$.

end

Stochastic approx.: $S^{k+1} \leftarrow S^k + \rho^k [S(z^{k+1}) - S^k]$.

Maximization: $\theta^{k+1} \leftarrow \theta^*(S^{k+1})$.

Increment: set $k \leftarrow k + 1$.

until convergence;

output: Estimation of θ^* .

Samples $(z^s)^s$ approximately distributed following $q(z|y, \theta^*)$.

$p(\mathbf{z}|\mathbf{y}, \theta)$. Therefore, we use a stochastic version of the EM algorithm coupled with a Monte-Carlo Markov-Chain method, namely, the Monte-Carlo Markov-Chain Stochastic Approximation Expectation-Maximization (MCMC-SAEM) algorithm that is able to deal with non-linear equations in a high-dimensional setting. The algorithm is proven to convergence (29) if the model belongs to the exponential family. In our case, it corresponds to consider that $p^{d_k} \sim \mathcal{N}(\bar{p}, \sigma_p^2)$, $v^{d_k} \sim \mathcal{N}(\bar{v}, \sigma_v^2)$ and $\beta_k \sim \mathcal{N}(\bar{\beta}_k, \sigma_\beta^2)$.

This leads to consider $\mathbf{z} = ((\xi_i)_{1 \leq i \leq I}, (\tau_i)_{1 \leq i \leq I}, (s_i)_{1 \leq i \leq I}, (p^{d_k})_{1 \leq k \leq N_c}, (v^{d_k})_{1 \leq k \leq N_c}, (\beta_k)_{1 \leq k \leq N_c(K-1)})$ as the extended hidden variables and $\theta = (t_0, \bar{p}, \bar{v}, (\beta_k)_{1 \leq k \leq N_c(K-1)}, \sigma_\xi, \sigma_\tau, \sigma_{\bar{p}}, \sigma_{\bar{v}}, \sigma)$ as the parameters of the model. The latter introduces sufficient statistics S of the model that are functions of the observations \mathbf{y} and latent variables \mathbf{z} . The aim of such functions is to disentangle the maximization of the parameters θ and the simulation of the latent variables \mathbf{z} .

The pseudo-code of the algorithm, reproduced in **Algorithm 1**, shows the different steps of the optimization until convergence. For further information about the steps of the algorithm, the reader is referred to Ref. (29–31) and references therein.

2.5. Simulation Study

Since we introduce a new approach to deal with longitudinal data spatially distributed, we performed a simulation procedure to show both the legitimacy of the model used, and the effectiveness of the estimation procedure. To this end, we define a graph represented on the top left of **Figure 4**, representing a square mesh of 7 nodes per edge, thus 49 nodes in total. Among them, 9 equally distributed nodes represent the control nodes, in red on the figure. As we simulate data according to equation (3), we choose position and velocities across the node of the graph, as shown on the top right part of **Figure 4**. Then we simulated realizations $(\xi_i, \tau_i, (s_{ij})_{1 \leq j \leq N_s})_{1 \leq i \leq N}$ for 350 patients, from 4 to 12 visits each (2,980 visits in total) such that it represents 350 longitudinal trajectories of biomarkers spatially distributed. These

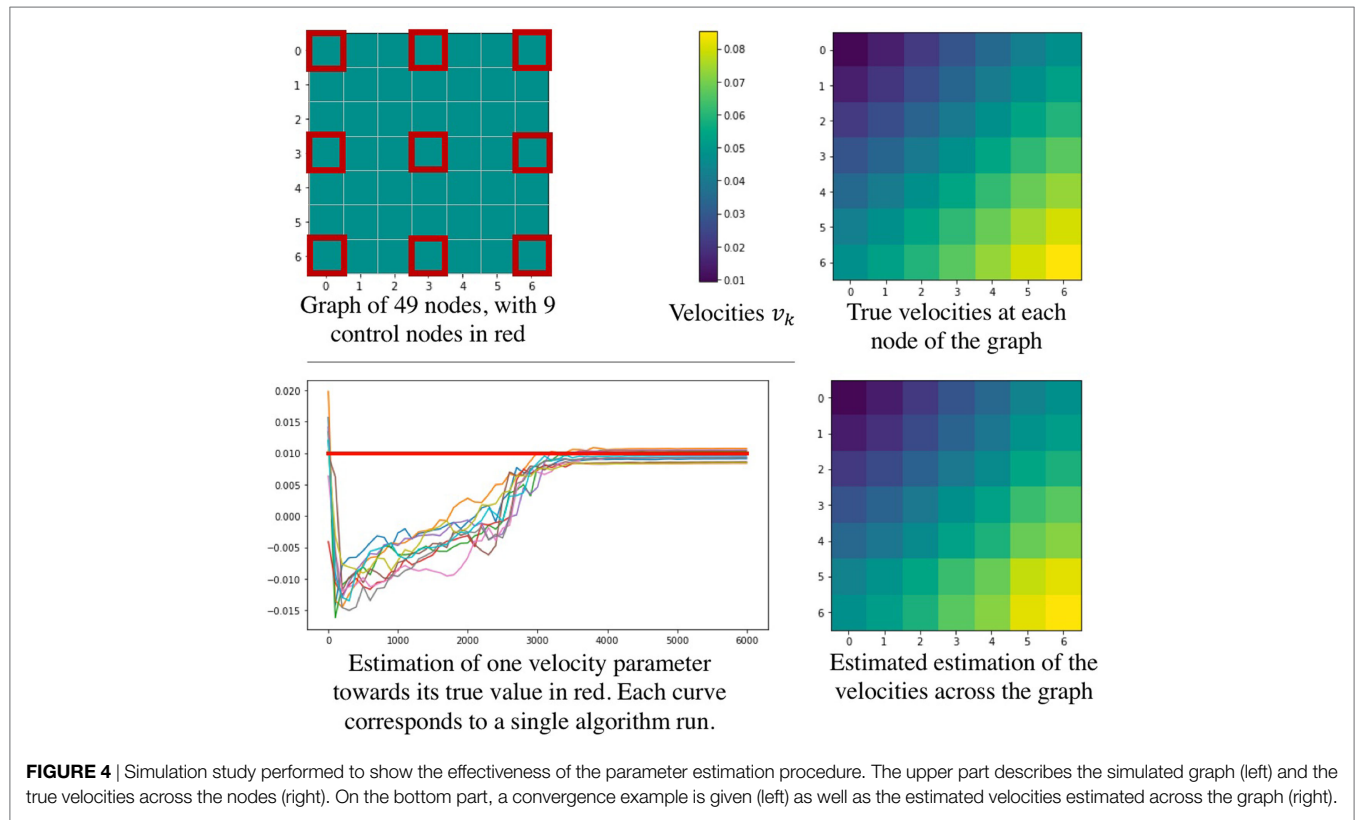


FIGURE 4 | Simulation study performed to show the effectiveness of the parameter estimation procedure. The upper part describes the simulated graph (left) and the true velocities across the nodes (right). On the bottom part, a convergence example is given (left) as well as the estimated velocities estimated across the graph (right).

TABLE 1 | The table shows the ability of the algorithm to estimate the real value of the model parameters.

Parameter	Initial value	Final value	Real value	Error rate (%)
ρ^{d_1}	2.0	2.994 (± 0.025)	3.0	0.2
$\rho^{d_{20}}$	2.0	3.663 (± 0.146)	3.714	1.4
$\rho^{d_{46}}$	2.0	3.860 (± 0.177)	3.9	1.0
v^{d_4}	1.0×10^{-2}	$2.84 (\pm 0.24) \times 10^{-2}$	3×10^{-2}	5.3
$v^{d_{21}}$	1.0×10^{-2}	$5.86 (\pm 0.49) \times 10^{-2}$	6.25×10^{-2}	6.2
$v^{d_{41}}$	1.0×10^{-2}	$7.83 (\pm 0.65) \times 10^{-2}$	7.8×10^{-2}	0.4
t_0	75	70.9 (± 2.7)	70	1.3
σ_τ^2	1.0×10^{-3}	27.5 (± 1.6)	25	10
σ_ξ^2	10^{-7}	0.154 (± 0.0008)	0.15	2.7
σ^2	Not initialized	$1.34 (\pm 0.03) \times 10^{-5}$	10^{-5}	34

data were used to find the parameters used to simulate them. Thus, we have performed 10 runs of the estimation procedure. In order to account for the stochasticity of the algorithm and the motion of the Markov Chains, the results in **Table 1** are given with their standard deviation over 10 runs. As we need an initial value for the parameters, we initialized the algorithm without specific knowledge about the positions and velocities, contrary to the experience on the cortical atrophy, so it might reflect a worst-case scenario. **Table 1** shows how well the algorithm performs on either control nodes or random nodes, as well as for the individual parameters.

The bottom part of **Figure 4** shows some results of the estimation procedure. On the left hand side, we provide an example of the stochastic estimations of a parameter over the iterations of the algorithm - the figure shows 10 independent runs. The right hand

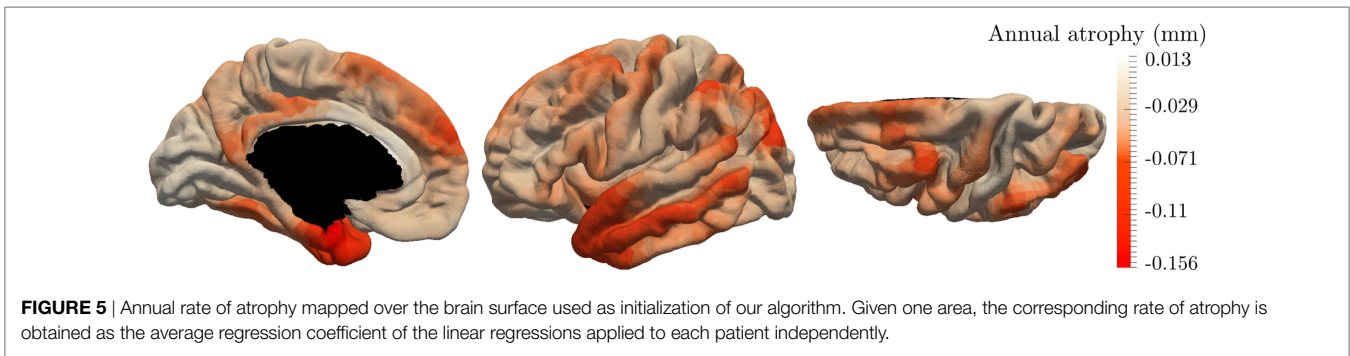
side presents the final estimation of the velocities across the node of the graph, showing that the model is likely to reproduce the real signal. Overall, these results confirm that such procedure seems reasonable to assess the validity of the model and of the estimation procedure in order to estimate the temporal profile of longitudinal data spatially distributed, such as the cortical atrophy.

3. RESULTS

3.1. Initialization

We evaluated the propagation of the cortical atrophy thanks to cortical thickness values of 154 MCI converters (787 observations) distributed on a graph with 1,827 nodes.

The initialization of the MCMC-SAEM algorithm requires initial values of the parameters θ and realizations \mathbf{z} . We would like to draw attention on the realizations $((\alpha_i)_{1 \leq i \leq I}, (\tau_i)_{1 \leq i \leq I}, (s_i)_{1 \leq i \leq I})$ and $((p^{d_k})_{1 \leq k \leq N_c}, (v^{d_k})_{1 \leq k \leq N_c}, t_0)$. The former are chosen equal to 0, leading to initial individual trajectories that are equal to the mean spatiotemporal trajectories. The pattern of atrophy is the same for everyone at the beginning. The latter variables, $((p^{d_k})_{1 \leq k \leq N_c}, (v^{d_k})_{1 \leq k \leq N_c}, t_0)$, are initialized based on the raw data. Besides t_0 that is chosen as the mean age of the input observations, for each control node k , we computed linear regressions on the longitudinal thickness values of each patient. Then we average the regression coefficients, each corresponding to a given subject, such that we end up with one rate of atrophy v_k per patch. Also, p_k was chosen as the average thickness on a given patch. **Figure 5** shows the map of the initial v_k distributed over the cortical surface which looks reasonable.



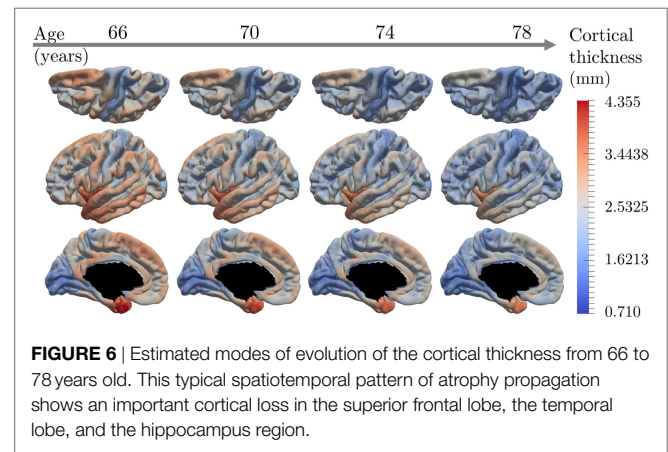
The initializations of **Figure 5** present areas with important cortical decrease over time, such as the temporal lobe and the hippocampus area. On the other hand, the primary visual cortex is less subject to a cortical atrophy. This initialization looks reasonable; however, these linear regressions are not able to reconstruct the individual observations, preventing from a characterization of personalized patterns of atrophy. It avoids describing the temporal and spatial variability of the individual propagations. Moreover, the linear regressions do not take into account the spatial coherence of the propagation as shown by the color-bar on **Figure 5** where some areas present an important increase of the cortical thickness. It may be associated to the important noise within the data which is produced by the data acquisition, the extraction of the cortical thickness, and, the alignment on the same atlas.

Thanks to the model we introduced, we were able to reconstruct a mean (resp. individual) spatiotemporal trajectory, detailed in section 3.2 (resp. 3.3), that takes the form of the input measurements, preventing from working with percentiles or clusters that cannot be compared directly to the real observations. Due to the numerous number of hyperparameters and the stochastic behavior of the MCMC-SAEM, the algorithm was computed several times, each run of 100,000 iterations taking approximately 15 h. The runs led to similar results. In the following, the results are presented for the run that provided the best individual reconstruction, i.e., the smaller standard deviation σ of the noise. Its last estimation is of 0.29 mm, where 90% of the input data are between 1.5 and 4 mm.

3.2. Population Level

The model exhibits a long-term characteristic pattern of atrophy propagation from early MCI stage to post AD diagnosis. It corresponds to the group-average trajectory described in section 2.3.1 whose spatial (w_i) and temporal (α_i and τ_i) variations corresponds to individual spatiotemporal trajectories. It is important to mention that this trajectory is a mean trajectory in a statistical sense, as its parameters are the mean values of the individual parameters.

Figure 6 shows the temporal and spatial evolution of the cortical atrophy, from 66 to 78 years old. The brain medial and lateral views shows an important atrophy on the temporal lobe and the medial temporal lobe, especially the fusiform and the parahippocampal gyrus. An important cortical decrease is also discernible on the superior frontal gyrus and at the wider region defined by the inferior parietal lobe and the angular gyrus. On

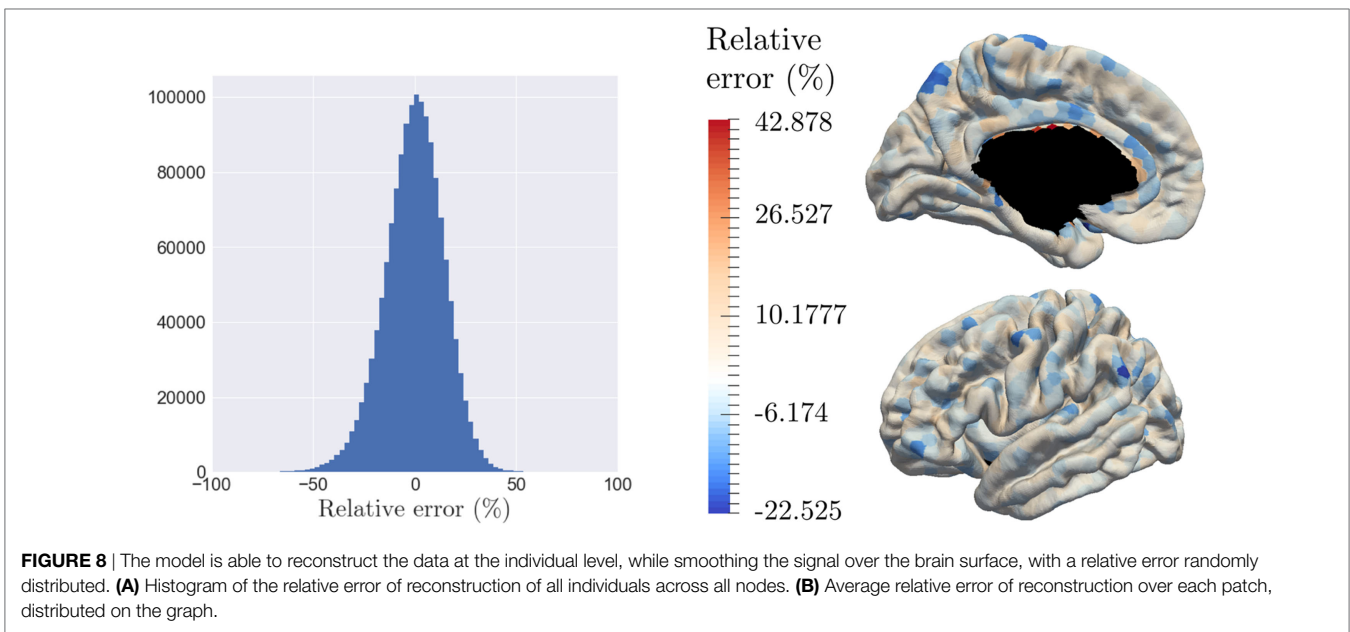
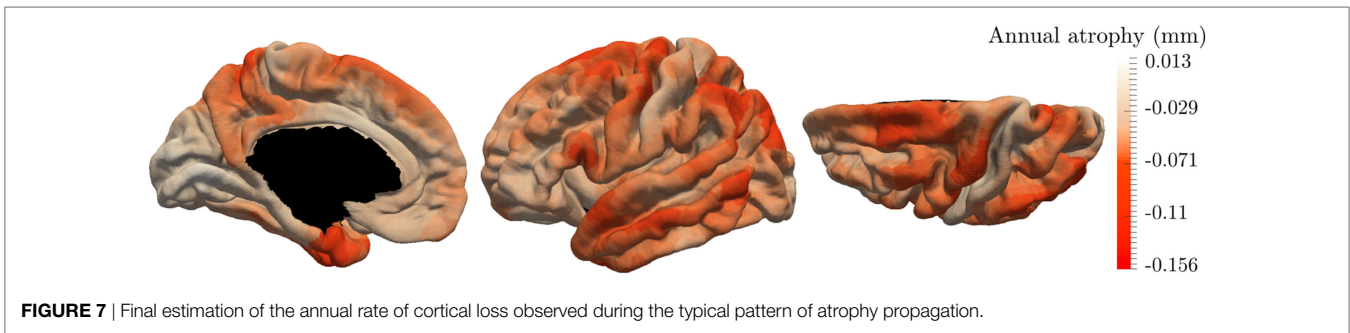


the other side, the prefrontal cortex, the primary visual cortex, the calcaris sulcus, and the post central gyrus are less subject to atrophy.

These results are supported by **Figure 7** that shows the map of the annual atrophy v_k for the mean spatiotemporal trajectory, distributed over the corresponding brain areas. The areas affected by the cortical atrophy correspond to previous knowledge (32–34) even though the different measurements and methodologies lack in consensus. The patterns are still debated in order to find the best characterization of AD compared to normal aging or other neurodegenerative diseases. The proposed model may provide results for different populations on the same atlas, facilitating the comparison between diseases or with normal aging.

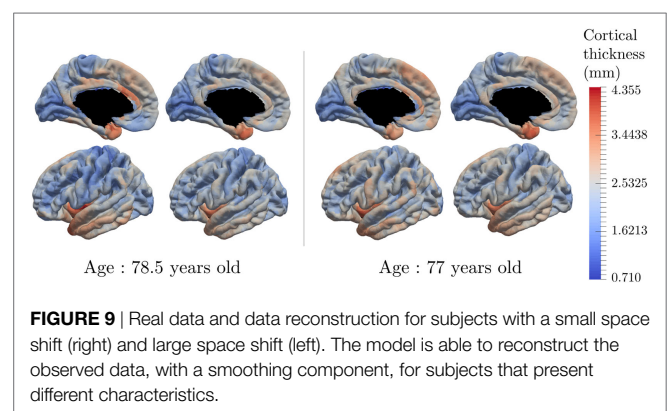
3.3. Individual Reconstruction

The model is able to characterize personalized patterns of atrophy propagation thanks to a reconstruction of the individual observations. The validation is assessed thanks to the relative error of reconstruction. As mentioned previously, the input data are noisy, at both a temporal and spatial level. As for the temporal part, the 154 patients represent 281.358 temporal profiles (time-series) over the 1,827 patches, from which only 6.4% present a monotonous profile of decrease. Given all the linear regression computed for the algorithm initialization, the mean (resp. the variance) of the corresponding R-square values is equal to 0.348 (resp. 0.307). On the other side, the spatial noise corresponds to high variation of the signal for neighbor nodes. Given this important noise, the goal of the reconstruction is not to reconstruct



perfectly the data but rather to smooth the propagation over the brain and to capture individual tendencies of atrophy propagation. Thus, the 787 observations involve 1,437,849 reconstruction y_{ijk} , whose relative error of reconstruction is represented on **Figure 8A** which confirms the hypothesis that the noise is a Gaussian distribution with a zero mean (p -value = $4.24 \cdot 10^{-109}$ for a t -test comparison with a theoretical distribution of mean equal to zero). As highlighted by **Figure 8B**, that represents the relative error of reconstruction over the 1,827 patches, the error is mostly randomly distributed over the brain surface. It confirms that the reconstruction error does not have a spatial component as it is uniformly distributed over the brain surface. The color-bar was chosen according to the extreme values: it is important to mention that the larger error of reconstruction corresponds to areas that are close to the corpus callosum where the interpolation relies on a fewer number of control points.

Figure 9 presents the reconstruction of two different individuals who present various individual spatiotemporal trajectory, especially space shift norms that are either in the 10% bigger on the left hand side, or in the 10% smaller on the right hand side. The left part of each individual part corresponds to the input data whereas the right part is the corresponding reconstruction done by the model. It shows that the reconstruction is likely to represent the real data. The same color-bar was used as for **Figure 6** to compare



the individual data with the characteristic pattern of atrophy. Moreover, the spatiotemporal trajectory η_i of individual i is not estimated only at the observed time-points but it is a continuous function of the time, as shown on **Figure 3C**. Therefore, it is possible to reconstruct the observation at any point, potentially in the future.

One of the properties of the model is to exhibit individual temporal parameters, namely the acceleration factor α_i and the time-shift τ_i , which allow to reparametrize the individual

dynamics on a common time-line. As the data used here correspond to the cortical thickness, the realignment is estimated thanks to structural biomarker dynamics. On the other side, the MCI converters have an age at disease onset, t_{diag} , which corresponds to a clinical status. The latter is not straightforwardly related to the structural dynamics of the individual. In that sense, we decided to realign the age at onset t_{diag} , a clinical biomarker, on the same time-line, assessed with the

structural biomarkers. The observed age at diagnosis $t_{diag,i}$ are represented by the red histogram on **Figure 10**, which is not unimodal and present an important variance. The realignment of the clinical status is represented thanks to the distribution of $(\psi_i(t_{diag,i}))_{1 \leq i \leq I}$, which is centered with a reduced variance. It suggests that the clinical conversion to AD, determined with t_{diag} corresponds to a specific stage of the cortical atrophy.

As the model estimates individual spatiotemporal trajectories, it allows to describe the variability within the population. The distributions of $(\alpha_i)_{1 \leq i \leq I}$, $(\tau)_{1 \leq i \leq I}$ and $(w_i)_{1 \leq i \leq I}$ account for the distribution of the individual patterns of atrophy. Furthermore, the ADNI dataset provides, for each patient, multiple features, such as the number of alleles of the APOE- $\epsilon 4$ gene, the gender, the marital status, and the educational level. In the case of the APOE- $\epsilon 4$ gene, which is known as a genetic risk factor regarding AD (35, 36), we exhibited the distribution of $(\alpha_i)_{1 \leq i \leq I}$ and $(\tau_i)_{1 \leq i \leq I}$ for the subpopulations defined by the number of alleles of the gene as shown on **Figure 11**. The more alleles, the more likely to have AD (35, 37).

As shown on the left hand side of **Figure 11**, the patients with two alleles (resp. one allele) present a mean time-shift of -2.98 years (resp. -0.20 years) after the mean scenario, contrary to patient without APOE- $\epsilon 4$ alleles that present an average time-shift of 1.89 years, meaning that the more alleles, the earlier the atrophy onset occurs. However, we applied Mann-Whitney two-sided statistical tests that lead to insignificantly differences between the subpopulation. On the other side, same tests were conducted for the same subpopulation with the mean acceleration factor whose distributions are presented on the right hand side of **Figure 11**. In this case, the group of individual with no alleles presented an average acceleration factor of 0.780, statistically different from the group of individual with one alleles (resp. two alleles) that presented an average acceleration factor of 1.415 (resp. 1.236) with a p -value equal to 0.00104 (resp. 0.00511). However,

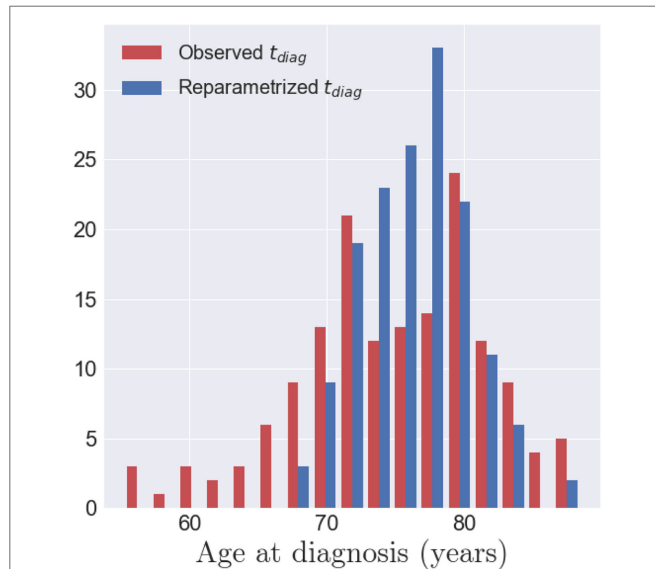


FIGURE 10 | In red, the histogram of the observed age at diagnosis $t_{diag,i}$ for the 154 MCI converters. In blue, the histogram of the reparametrized age at diagnosis $\psi_i(t_{diag,i})$ once aligned on the common time-line. This shows that the age at diagnosis is mapped to a smaller range of time-points, in the model of cortical atrophy, suggesting that conversion to AD occurs at a specific stage of cortical atrophy.

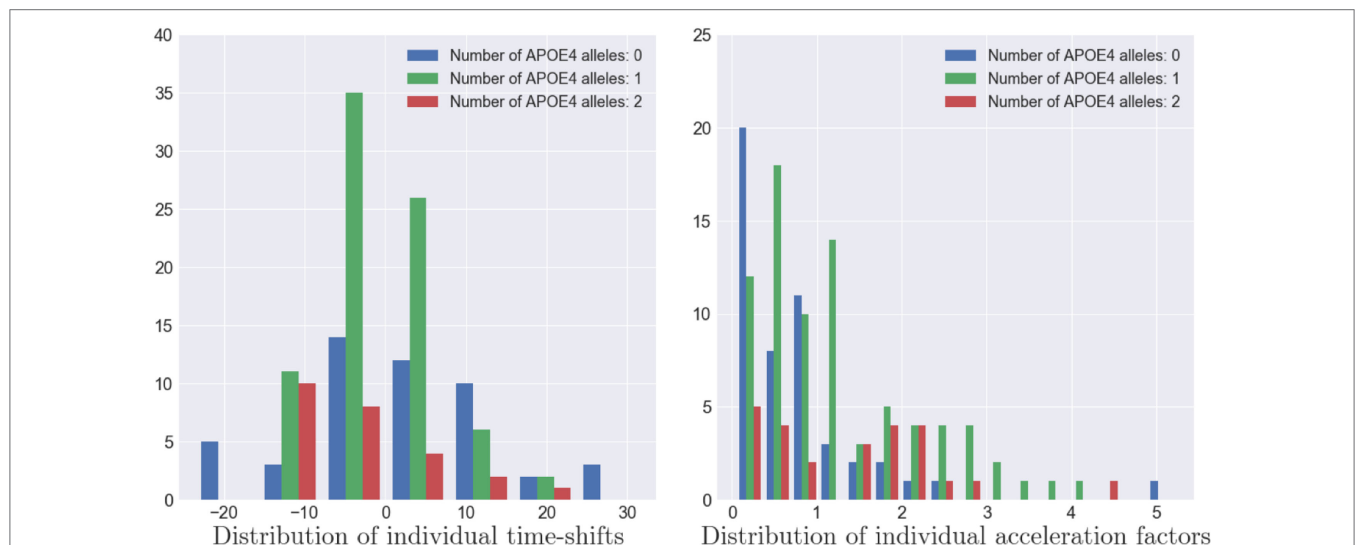


FIGURE 11 | Distribution of the individual time-shifts (left) and the individual acceleration factors (right) for three types of APOE- $\epsilon 4$ population. A larger number of alleles of the APOE- $\epsilon 4$ genes is correlated to a faster pace of propagation of the Alzheimer's disease (p -value $\simeq 0.001$) but not with an earlier atrophy onset (p -value $\simeq 0.5$).

this acceleration factor is not statistically different between the population with one or two alleles (p -value = 0.51518), meaning that these subpopulation have similar rate of atrophy. Additional investigation on the gender, the marital status and the education level did not led to significant differences. It is important to mention that the Mann–Whitney test is sensitive to the number of samples whereas this study focuses on only 154 MCI patients that might lead to insignificant results in some cases, particularly in the case of the educational level (20 categories) or the marital status (unbalanced classes). Finally, it should mentioned that the tests conducted on the individual space shifts w_i and the related sources s_i did not lead to significant results, mainly because these parameters account for the difference in brain size, and thus thickness, between people.

4. DISCUSSION

The paper presents a mixed-effects model of the atrophy propagation that is able to characterize a typical pattern of propagation, and, that reconstructs individual observations and scenarios of atrophy. The model exhibits brain areas that are the most affected by the cortical atrophy, such as the parahippocampal gyrus, the temporal lobe, and the superior frontal gyrus. The lesions are less important in the primary visual cortex, the prefrontal cortex, and the primary sensory cortex. The model allows to account for the different temporal dynamics of the alterations that can be then compared and ordered.

The proposed model offers a wide versatility of instantiation in terms of profile of temporal variations (exponential decay, sigmoid decay) and spatial variations (resolution, number of control nodes, kernel bandwidth) as it defines a generic framework for the estimation of longitudinal signals spatially distributed. It should be compared to other types of graph-related approaches, such as supervoxels (38) or a vertex-cluster method (39). The latter has exhibited clusters of regression that show profiles of atrophy similar to our results. However, such models do not deal with individual characteristics neither directly with imaging data but rather with normalized values or percentiles, which restrict the interpretation. Further efforts should be concentrated on the validation and improvement of our model, possibly with more complex data and signal propagation.

The individual reconstructions also inform about subject-specific patterns of atrophy propagation, with potential personalized estimation of the cortical atrophy at future time-points. Further investigations have to be conducted to ensure the quality of the new observations the model is able to generate, so that one can exploit the outcome that the model can predict for an individual some years after his or her last visit. This should be done with a proper validation set to determine the population parameters, and a test-set to predict the individual parameters and thus the future observations. Consistent results might provide information about the structural biomarkers related to the progression of AD, such as in Ref. (40).

Another improvement of the model relies in the distance matrix computation. In this paper, the distance between the nodes is related to the distance on the brain surface, hiding potential effects

of the neuronal connections. New distances might be computed based on functional connectivity or combination of different distances, in order to associate the functional and structural components of the brain that are supposed to be complementary in the disease process (41–43).

The model has the potential to exhibit the spatiotemporal propagation of any signal spatially distributed over a graph. It can be used in order to compare the patterns of propagation in distinct population, e.g., normal aging or any other neurodegenerative diseases. It is also a first step to define personalized patterns that would help for a future prognosis of the patient stages.

AUTHOR CONTRIBUTIONS

All authors listed have made substantial, direct and intellectual contribution to the work, and approved it for publication.

ACKNOWLEDGMENTS

Data collection and sharing for this project was funded by the Alzheimer's Disease Neuroimaging Initiative (ADNI) (National Institutes of Health Grant U01 AG024904) and DOD ADNI (Department of Defense award number W81XWH-12-2-0012). ADNI is funded by the National Institute on Aging, the National Institute of Biomedical Imaging and Bioengineering, and through generous contributions from the following: AbbVie, Alzheimer's Association; Alzheimer's Drug Discovery Foundation; Araclon Biotech; BioClinica, Inc.; Biogen; Bristol-Myers Squibb Company; CereSpir, Inc.; Cogstate; Eisai Inc.; Elan Pharmaceuticals, Inc.; Eli Lilly and Company; EuroImmun; F. Hoffmann–La Roche Ltd and its affiliated company Genentech, Inc.; Fujirebio; GE Healthcare; IXICO Ltd.; Janssen Alzheimer Immunotherapy Research & Development, LLC.; Johnson & Johnson Pharmaceutical Research & Development LLC.; Lumosity; Lundbeck; Merck & Co., Inc.; Meso Scale Diagnostics, LLC.; NeuroRx Research; Neurotrack Technologies; Novartis Pharmaceuticals Corporation; Pfizer Inc.; Piramal Imaging; Servier; Takeda Pharmaceutical Company; and Transition Therapeutics. The Canadian Institutes of Health Research is providing funds to support ADNI clinical sites in Canada. Private sector contributions are facilitated by the Foundation for the National Institutes of Health (www.fnih.org). The grantee organization is the Northern California Institute for Research and Education, and the study is coordinated by the Alzheimer's Therapeutic Research Institute at the University of Southern California. ADNI data are disseminated by the Laboratory for Neuro Imaging at the University of Southern California.

FUNDING

This work has been partly funded by the European Research Council (ERC) under grant agreement No. 678304, European Union's Horizon 2020 research and innovation program under grant agreement No. 666992, and the program "Investissements d'avenir" ANR-10-IAIHU-06.

REFERENCES

- Du AT, Schuff N, Amend D, Laakso MP, Hsu YY, Jagust WJ, et al. Magnetic resonance imaging of the entorhinal cortex and hippocampus in mild cognitive impairment and Alzheimer's disease. *J Neurol Neurosurg Psychiatry* (2001) 71(4):441–7. doi:10.1136/jnnp.71.4.441
- Benzinger TL, Blazey T, Jack CR, Koeppe RA, Su Y, Xiong C, et al. Regional variability of imaging biomarkers in autosomal dominant Alzheimer's disease. *Proc Natl Acad Sci U S A* (2013) 110(47):E4502–9. doi:10.1073/pnas.1317918110
- Amieva H, Le Goff M, Millet X, Orgogozo JM, Pérès K, Barberger-Gateau P, et al. Prodromal Alzheimer's disease: successive emergence of the clinical symptoms. *Ann Neurol* (2008) 64(5):492–8. doi:10.1002/ana.21509
- Wilson R, Leurgans S, Boyle P, Bennett D. Cognitive decline in prodromal Alzheimer disease and mild cognitive impairment. *Arch Neurol* (2011) 68(3):351–6. doi:10.1001/archneurol.2011.31
- Mura T, Proust-Lima C, Jacqmin-Gadda H, Akbaraly TN, Touchon J, Dubois B, et al. Measuring cognitive change in subjects with prodromal Alzheimer's disease. *J Neurol Neurosurg Psychiatry* (2014) 85(4):363–70. doi:10.1136/jnnp-2013-305078
- Jack CR, Knopman DS, Jagust WJ, Shaw LM, Aisen PS, Weiner MW, et al. Hypothetical model of dynamic biomarkers of the Alzheimer's pathological cascade. *Lancet Neurol* (2010) 9(1):119–28. doi:10.1016/S1474-4422(09)70299-6
- Fan Y, Resnick M, Wu X, Davatzikos C. Structural and functional biomarkers of prodromal Alzheimer's disease: a high dimensional pattern classification study. *Neuroimage* (2008) 41(2):277–85. doi:10.1016/j.neuroimage.2008.02.043
- Singh V, Chertkow H, Lerch JP, Evans AC, Dorr AE, Kabani NJ. Spatial patterns of cortical thinning in mild cognitive impairment and Alzheimer's disease. *Brain* (2006) 129(11):2885. doi:10.1093/brain/awl256
- Baron J, Chételat G, Desgranges B, Perchev G, Landeau B, de la Sayette V, et al. In vivo mapping of gray matter loss with voxel-based morphometry in mild Alzheimer's disease. *Neuroimage* (2001) 14(2):298–309. doi:10.1006/nimg.2001.0848
- Fonteijn HM, Modat M, Clarkson MJ, Barnes J, Lehmann M, Hobbs NZ, et al. An event-based model for disease progression and its application in familial Alzheimer's disease and huntington's disease. *Neuroimage* (2012) 60(3):1880–9. doi:10.1016/j.neuroimage.2012.01.062
- Young AL, Oxtoby NP, Daga P, Cash DM, Fox NC, Ourselin S, et al. A data-driven model of biomarker changes in sporadic Alzheimer's disease. *Brain* (2014) 137(9):2564–77. doi:10.1093/brain/awu176
- Young AL, Oxtoby NP, Huang J, Marinescu RV, Daga P, Cash D, et al. Multiple orderings of events in disease progression. *Information Processing in Medical Imaging*. Isle of Skye, Scotland: Springer (2015). p. 711–22.
- Jedynak BM, Lang A, Liu B, Katz E, Zhang Y, Wyman BT, et al. A computational neurodegenerative disease progression score: method and results with the Alzheimer's disease neuroimaging initiative cohort. *Neuroimage* (2012) 63(3):1478–86. doi:10.1016/j.neuroimage.2012.07.059
- Donohue M, Jacqmin-Gadda H, Goff ML, Thomas R, Raman R, Gams A, et al. Estimating long-term multivariate progression from short-term data. *Alzheimers Dement* (2014) 10(5):400–10. doi:10.1016/j.jalz.2013.10.003
- Gao S, Hendrie H, Hall K, Hui S. The relationships between age, sex, and the incidence of dementia and Alzheimer disease: a meta-analysis. *Arch Gen Psychiatry* (1998) 55(9):809–15. doi:10.1001/archpsyc.55.9.809
- Devanand DP, Pradhaban G, Liu X, Khandji A, De Santi S, Segal S, et al. Hippocampal and entorhinal atrophy in mild cognitive impairment: prediction of Alzheimer disease. *Neurology* (2007) 68(11):828–36. doi:10.1212/01.wnl.0000256697.20968.d7
- Bilgel M, Prince JL, Wong DF, Resnick SM, Jedynak BM. A multivariate nonlinear mixed effects model for longitudinal image analysis: application to amyloid imaging. *Neuroimage* (2016) 134:658–70. doi:10.1016/j.neuroimage.2016.04.001
- Schiratti J-B, Allassonnière S, Colliot O, Durrleman S. Learning spatiotemporal trajectories from manifold-valued longitudinal data. In: Cortes C, Lawrence ND, Lee DD, Sugiyama M, Garnett R, editor. *Advances in Neural Information Processing Systems*. Curran Associates, Inc (2015). p. 2404–12.
- Durrleman S, Pennec X, Trouvé A, Braga J, Gerig G, Ayache N. Toward a comprehensive framework for the spatiotemporal statistical analysis of longitudinal shape data. *Int J Comput Vis* (2013) 103(1):22–59. doi:10.1007/s11263-012-0592-x
- Leuchter AF, Newton TF, Cook IA, Walter DO, Rosenberg-Thompson S, Lachenbruch PA. Changes in brain functional connectivity in Alzheimer-type and multi-infarct dementia. *Brain* (1992) 115(5):1543–61. doi:10.1093/brain/115.5.1543
- Maguire EA, Burgess N, Donnett JG, Frackowiak RSJ, Frith CD, O'Keefe J. Knowing where and getting there: a human navigation network. *Science* (1998) 280(5365):921–4. doi:10.1126/science.280.5365.921
- Broomhead DS, Lowe D. *Radial Basis Functions, Multi-Variable Functional Interpolation and Adaptive Networks*. Technical report. United Kingdom: Royal Signals and Radar Establishment Malvern (1988).
- Reuter M, Schmandsky N, Rosas H, Fischl B. Within-subject template estimation for unbiased longitudinal image analysis. *Neuroimage* (2012) 61(4):1402–18. doi:10.1016/j.neuroimage.2012.02.084
- Fischl B, Sereno M, Tootell R, Dale A. High-resolution intersubject averaging and a coordinate system for the cortical surface. *Human Brain Mapp* (1999) 8:272–84. doi:10.1002/(SICI)1097-0193(1999)8:4<272::AID-HBM10>3.0.CO;2-4
- Peyré G, Péchaud M, Keriven R, Cohen LD. Geodesic methods in computer vision and graphics. *Found Trends Comp Graph Vis* (2010) 5(3–4):197–397. doi:10.1561/06000000029
- Schiratti J-B, Allassonnière S, Colliot O, Durrleman S. A bayesian mixed-effects model to learn trajectories of changes from repeated manifold-valued observations. *J Mach Learn Res* (2017) 18(133):1–33.
- Allassonnière S, Younes L. A stochastic algorithm for probabilistic independent component analysis. *Ann Appl Stat* (2012) 6(1):125–60. doi:10.1214/11-AOAS499
- Dempster AP, Laird NM, Rubin DB. Maximum likelihood from incomplete data via the em algorithm. *J R Stat Soc Ser B* (1977) 39:1–38.
- Allassonnière S, Kuhn E, Trouvé A. Construction of bayesian deformable models via a stochastic approximation algorithm: a convergence study. *Bernoulli* (2010) 16(3):641–78. doi:10.3150/09-BEJ229
- Delyon B, Lavielle M, Moulines E. Convergence of a stochastic approximation version of the em algorithm. *Ann Stat* (1999) 27:94–128.
- Kuhn E, Lavielle M. Maximum likelihood estimation in nonlinear mixed effects models. *Comput Stat Data Anal* (2005) 49(4):1020–38. doi:10.1016/j.csda.2004.07.002
- Whitwell JL, Przybelski SA, Weigand SD, Knopman DS, Boeve BF, Petersen RC, et al. 3d maps from multiple mri illustrate changing atrophy patterns as subjects progress from mild cognitive impairment to Alzheimer's disease. *Brain* (2007) 130(7):1777–86. doi:10.1093/brain/awm112
- Jack CR, Petersen RC, Xu YC, Waring SC, O'Brien PC, Tangalos EG, et al. Medial temporal atrophy on mri in normal aging and very mild Alzheimer's disease. *Neurology* (1997) 49(3):786–94. doi:10.1212/WNL.49.3.786
- Scahill RI, Schott JM, Stevens JM, Rossor MN, Fox NC. Mapping the evolution of regional atrophy in Alzheimer's disease: unbiased analysis of fluid-registered serial mri. *Proc Natl Acad Sci U S A* (2002) 99(7):4703–7. doi:10.1073/pnas.052587399
- Strittmatter WJ, Saunders AM, Schmechel D, Pericak-Vance M, Enghild J, Salvesen GS, et al. Apolipoprotein e: high-avidity binding to beta-amyloid and increased frequency of type 4 allele in late-onset familial Alzheimer disease. *Proc Natl Acad Sci U S A* (1993) 90(5):1977–81. doi:10.1073/pnas.90.5.1977
- Poirier J, Bertrand P, Kogan S, Gauthier S, Davignon J, Bouthillier D. Apolipoprotein e polymorphism and Alzheimer's disease. *Lancet* (1993) 342(8873):697–9. doi:10.1016/0140-6736(93)91705-Q
- Corder E, Saunders A, Strittmatter W, Schmechel D, Gaskell P, Small G, et al. Gene dose of apolipoprotein e type 4 allele and the risk of Alzheimer's disease in late onset families. *Science* (1993) 261(5123):921–3. doi:10.1126/science.8346443
- Segovia F, Górriz J, Ramírez J, Salas-Gonzalez D, Álvarez I, López M, et al. A comparative study of feature extraction methods for the diagnosis of Alzheimer's disease using the adni database. *Neurocomputing* (2012) 75(1):64–71. doi:10.1016/j.neucom.2011.03.050
- Marinescu RV, Eshaghi A, Lorenzi M, Young AL, Oxtoby NP, Garbarino S, et al. A vertex clustering model for disease progression: application to cortical thickness images. *International Conference on Information Processing in Medical Imaging*. Boone, NC: Springer (2017). p. 134–45.
- Eskildsen SF, Coupé P, Fonov VS, Pruessner JC, Collins DL, Initiative ADN, et al. Structural imaging biomarkers of Alzheimer's disease: predicting disease

- progression. *Neurobiol Aging* (2015) 36:S23–31. doi:10.1016/j.neurobiolaging.2014.04.034
41. Bullmore E, Sporns O. Complex brain networks: graph theoretical analysis of structural and functional systems. *Nat Rev Neurosci* (2009) 10(3):186–98. doi:10.1038/nrn2618
 42. Damoiseaux JS, Greicius MD. Greater than the sum of its parts: a review of studies combining structural connectivity and resting-state functional connectivity. *Brain Struct Funct* (2009) 213(6):525–33. doi:10.1007/s00429-009-0208-6
 43. Wee C-Y, Yap P-T, Zhang D, Denny K, Browndyke JN, Potter GG, et al. Identification of mci individuals using structural and functional connectivity networks. *Neuroimage* (2012) 59(3):2045–56. doi:10.1016/j.neuroimage.2011.10.015

Conflict of Interest Statement: The authors declare that the research was conducted in the absence of any commercial or financial relationships that could be construed as a potential conflict of interest.

Copyright © 2018 Koval, Schiratti, Routier, Bacci, Colliot, Allasonnière and Durrleman. This is an open-access article distributed under the terms of the Creative Commons Attribution License (CC BY). The use, distribution or reproduction in other forums is permitted, provided the original author(s) and the copyright owner are credited and that the original publication in this journal is cited, in accordance with accepted academic practice. No use, distribution or reproduction is permitted which does not comply with these terms.